Multilayer Modeling of Reflectance Pulse Oximetry

James L. Reuss, *Senior Member, IEEE*

***Abstract*—A multilayer tissue description was employed in Monte Carlo simulations of reflectance pulse oximetry to study the impact of assumptions made in previous studies employing homogeneous tissue models. Simulation results with a discrete layer of arterial pulsatility were similar to previous studies employing homogenous tissue models. However, the relationship of normalized pulse amplitude to emitter-detector spacing reiterates that spacing has a significant impact on pulse oximetry function. The effect of melanin content as a thin, superficial absorber was also simulated, with results supporting the general clinical observation that skin shade need not substantially compromise pulse oximeter accuracy.**

***Index Terms*—Fetal surveillance, Monte Carlo simulation, reflectance pulse oximetry, tissue optics.**

I. Introduction

PULSE oximetry, the noninvasive measurement of arterial oxygen saturation (SpO_2), has become a standard of care in many areas of clinical practice [1]. After initial success in operative and critical care monitoring of adults and neonates, development has focused on overcoming the limitations of low perfusion and motion, and exploring new applications such as intrapartum fetal pulse oximetry [2].

Several factors have made fetal pulse oximetry a challenging application. The fetus functions at a broad, low oxygen saturation range of $\mathrm{SaO}_2 = 40\%$–75%, with clinically significant desaturations occurring below 30% [3]. Commercially available fetal pulse oximeters employ sensors operating in reflectance mode, placed via the birth canal upon the fetus during labor [4]. Stability of tissue characteristics at the monitoring site, blood fraction in particular, becomes more critical at low saturations [5]. The many factors influencing the accuracy and availability of fetal oxygen saturation measurement [6] are difficult to investigate *in vivo*, especially in clinical practice. This has stimulated interest in mathematical modeling of light in tissue to gain insight into the phenomena underlying pulse oximetry.

II. Background

Modeling of the interaction of light with physiological tissue is motivated by a need to understand and predict the function and limitations of various light-based medical technologies. The Beer–Lambert law approximation of pulse oximetry considers only absorption by the medium. Although hemoglobin solutions obey Beer's law, red blood cells in solution do not [7]. Nonetheless, it yields the ratiometric approach to oxygen saturation calculation; empirical calibration removes the effects of other tissue characteristics as long as they remain close to their state at calibration. Kubelka–Munk theory incorporated scattering in a heuristic approach to deriving optical density, and was applied to *in vitro* and *in vivo* oximetry [8]; however, its assumption of isotropic scattering was unrealistic. Twersky's multiple scattering theory has been the most successful basis for modeling whole blood [9] for *in vitro* oximetry.

The photon diffusion (PD) model [10], incorporating the effects of anisotropic scattering by different tissue components, more accurately reflects the tissue characteristics. Schmitt derived approximate analytical solutions from PD theory for a homogeneous tissue model of both reflectance and transmission pulse oximetry [11]. Marble found *in vivo* results for a transmission mode sensor followed PD model predictions closely [12]. Takatani [13] and Schmitt [14] also obtained the analytical PD solutions for two-layer and three-layer tissue descriptions, with simplifying assumptions.

A tissue model of complexity sufficient to approximate mammalian skin tissue with pulsatile blood flow requires multiple layers with unique optical properties, reflecting the heterogeneous distribution of blood in tissue. A four-layer tissue model used by van Gemert in studying laser dosimetry incorporated a layer representing a blood plexus [15], but an analytical solution was not published.

Monte Carlo (MC) simulation can model light behavior in arbitrarily complex tissue structures. Inexpensive computing capability has removed a major obstacle to its successful use. Graaff employed MC simulation of light traveling through a homogeneous, single-layer tissue model to demonstrate the importance of light scattering in understanding reflectance pulse oximetry [16]. Tuchin used MC methods to solve the inverse problem of obtaining optical parameters from tissue samples based upon a five-layer model [17].

Results have not been published for pulse oximetry models with a tissue description close to the anatomical complexity of skin. Nonetheless, simpler pulse oximetry models illustrate the importance of understanding the behavior of light in tissue and how tissues characteristics impact device performance [18].

III. Methodology

In this study, reflectance pulse oximetry was modeled by performing simulations of photon migration at multiple wavelengths through the tissue for the diastolic and systolic states at a given set of tissue characteristics, including arterial oxygen saturation. The systolic state was obtained by an incremental increase of arterial blood over the diastolic state.

Multiple-layer simulation results were compared to results for the single-layer volume that results from "homogenizing" the constituents of the multiple-layer tissue volume. Results were studied over a range of emitter-detector spacing referred

Manuscript received October 29, 2003; revised May 31, 2004.

The author is with OB Scientific, Inc., N112 W18741 Mequon Rd., Germantown, WI 53022, USA (e-mail: jim.reuss@obscientific.com; jamesreuss@ieee.org).

Digital Object Identifier 10.1109/TBME.2004.840188

TABLE I
OPTICAL CHARACTERISTICS OF THE TISSUE CONSTITUENTS

var.	meaning	660 nm	890 nm
$\mu_a(HHb)$	absorption, deoxygenated Hb	17.139	4.595
$\mu_a(O_2Hb)$	absorption, oxygenated Hb	1.692	6.309
$\mu_a(tissue)$	absorption, non-blood tissue	0.285	0.245
$\mu_a(melanin)$	absorption, melanin	269.440	99.558
μ_s	scattering, blood & tissue	71.5	44.5
g	anisotropy	0.8	
n	refractive indices (internal)	1.3	

herein as the *far-detector* condition, greater than 0.5 cm, which is most typical of pulse oximetry sensor designs.

A. Tissue Model

The total blood fraction f_0 (nominal 5%; reduced 1.25%) is the mean concentration of blood in the total tissue volume during the diastolic state. The arterial pulsation was simulated by displacement of nonblood tissue by the added arterial blood. The pulse fraction f_p (nominal 0.25%; reduced 0.0625%) is the fraction of the *total tissue volume* displaced by the arterial pulse. The arterial oxygen saturation SaO_2 was varied in steps between 20% and 100%, with the venous oxygen saturation SvO_2 set 10% lower. The values of f_A (25%) and f_V (75%) correspond to the diastolic state.

Table I contains the optical characteristics, including absorbance, μ_a (cm^{-1}), and scattering μ_s (cm^{-1}), for blood versus nonblood tissue. The values of the absorbance for deoxygenated and oxygenated hemoglobin, μ_a (HHb) and $\mu_a(O_2Hb)$, respectively, were taken from the absorbance spectra published by Takatani [13]. The scattering coefficient for nonblood tissue and blood, μ_s, was derived from the reduced scattering coefficient, μ_s', as interpolated by Mannheimer [18] from observations of Schmitt [11]. The nonblood tissue absorption coefficient $\mu_a(\text{tissue})$ was also from Schmitt. The absorbance of melanin, $\mu_a(\text{melanin})$, was calculated as a function of wavelength according to the approximation derived by Jacques [19] from his study of melanosome absorption [20].

The anisotropy g was assumed to be 0.8, in the range of approximately 0.7–0.9 identified for dermis exposed to light of the red-NIR range in the review of van Gemert [15]. Although certain components of the tissue volume such as collagen [21] and red blood cells [22] are more forward-scattering ($g > 0.95$), the value of 0.8 is more representative of overall dermal scattering. The refractive index n for all internal surface interfaces was assumed to be 1.3 (little specular reflectance at interfaces), with $n = 1.0$ at the surface interface ($z = 0$). It should be noted that the model layer interfaces are artificial, in that the actual structural interfaces in tissue (e.g., vessel walls) are at a finer level of detail than the model represents. The simplifying assumptions made here are similar to those used in other studies [11], [13], [18].

A multilayer description of mammalian skin tissue was derived from a simplified anatomy, shown in Fig. 1. The tissue model consists of six homogeneous layers, with different blood fractions. The layer number i runs from 1 (most shallow) to 6 (deepest). (The subscript zero denotes values of the single-layer model resulting from homogenization of the multilayer contents.) Each layer i is given a name suggestive of the corresponding anatomical structure. Layer thickness d_i, and blood fraction f_i for each layer in the diastolic state with nominal f_0 of 5% is found in Table II.

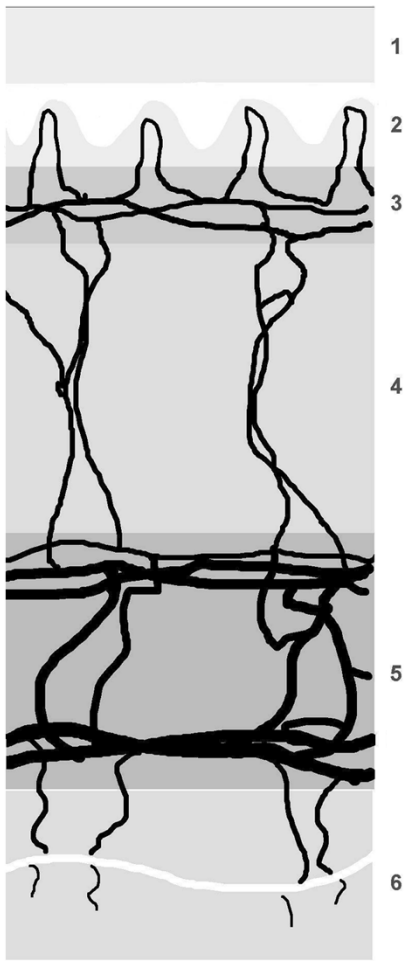

Fig. 1. Schematic of vasculature superimposed upon the multilayer model. Shading indicates relative absorbance; melanin not shown; not to scale.

TABLE II
MULTILAYER TISSUE MODEL FOR NOMINAL BLOOD FRACTION $f_0 = 0.05$

layer (i)	name	d_i (cm)	f_i
1	epidermis	0.02	0
2	dermis	0.02	0
3	papillary plexus	0.02	0.0556
4	dermis	0.08	0.0417
5	cutaneous plexus	0.06	0.2037
6	hypodermis	0.80	0.0417

Since each layer is uniformly thick, their relative volumes are expressed by their relative thicknesses d_i alone. The tissue model's geometry is similar to the five-layer skin model utilized by Tuchin [17], although the optical characteristics are different. The background tissue content of each layer is homogeneous; connective tissue, nerves, and other discrete structures are not individually represented.

The epidermal layer is defined to permit modeling of melanin content, f_{mel}. Melanin was omitted in order to facilitate comparisons between the single-layer model and the multilayer model. (The impact of melanin was investigated separately for $f_{\text{mel}} =$

5%, 10%, and 20%.) A blood- and melanin-free layer of dermis separates the epidermis from the papillary plexus. The papillary plexus has a somewhat higher blood fraction than the dermis below it, but this layer is microcirculatory, i.e., nonpulsatile.

The thickness of these superficial layers was set to 0.02 cm each. The epidermal thickness has been measured as low as 0.006 cm [19]. The 0.02 cm thickness helps ensure a sufficient number of grid elements per layer with a spatial resolution that would not pose an undue computational burden (see "Monte Carlo algorithm" below). Also, keeping simple ratios between the thinnest and thicker layers facilitated homogenization of the multilayer model into a single-layer equivalent.

The cutaneous plexus layer represents the capillary plexus, the arterioles supplying the entire tissue volume, and the venules collecting returning venous blood. This layer is the location of pulsatility in the tissue model. The incremental increase in arterial blood displaces nonblood tissue, without affecting the venous blood volume. This is consistent with the magnitude of the absorbance change measured in the photoplethysmographic signal, which cannot be explained merely by the rather small arterial-venous oxygen saturation difference occurring in the small fraction of blood representing the pulse. Obviously, the diastolic proportions of arterial and venous blood must be restored prior to the next arterial pulse, or venous congestion would result. This process may commence prior to the end of the arterial pulse, but the dynamics of the situation are beyond the scope of this simulation.

The thickness of the hypodermis implies the absence of subdermal reflectors (such as bone) in this model, and minimizes the loss due to transmission of photons that might otherwise scatter back to the surface ($z = 0$).

The relative blood fractions were defined in order to ensure that "homogenization" of the 6-layer model would result in a single layer, $d_0 = 1$ cm, with the predetermined diastolic blood fraction f_0, i.e.,

$$f_0 = \left(\sum_{i=1}^{6} d_i \times f_i \right) \Big/ d_0. \tag{1}$$

The 1:3 $f_A : f_V$ proportion applies to all layers in the diastolic state. Letting f_{iA} and f_{iV} represent the arterial and venous blood fractions of layer i, then in the diastolic state

$$f_{iA} = f_i \times f_A \tag{2}$$

and

$$f_{iV} = f_i \times f_V. \tag{3}$$

Letting f_{iAS} represent the arterial blood fraction of layer i in the systolic state, then for pulsatility in a single layer i_p,

$$f_{iAS} = f_{iA} \quad i \neq i_p \tag{4}$$

and

$$f_{iAS} = f_{iA} + (d_0/d_i) \times f_p \quad i = i_p. \tag{5}$$

A nominal diastolic blood fraction $f_0 = 0.05$ with nominal pulse fraction $f_p = 0.0025$ was compared to a reduced blood fraction $f_0' = 0.0125$ with reduced pulse fraction $f_p' = 0.000\,625$. The diastolic blood fraction reduction was applied uniformly to all layers, i.e., $f_i' = f_i \times (f_0'/f_0)$. The arterial pulsation was simulated by displacement of nonblood tissue of the cutaneous plexus layer ($i_p = 5$) by the added arterial blood. With $f_p = 0.0025$ in the cutaneous plexus layer, the arterial fraction becomes $f_{5AS} = 0.0926$, and $f_{5S} = 0.2454$. The nonblood tissue component of layer five is similarly reduced.

The absorbance by layer and wavelength was computed as the sum of arterial, venous, and nonblood absorbance values, weighted by their respective fractions in the layer.

B. Sensor Model

The simplified model of a reflectance pulse oximetry sensor consists of multiple co-located emitters, and a detector a variable distance away. The commonly used emitter wavelengths of 660 and 890 nm were used in the simulation. Emitters were simulated with a Gaussian beam profile of radius 0.3 cm. This approximates a noncollimated light-emitting diode (LED). The detector was modeled as a square $d = 0.2$ cm. The emitter-detector spacing r_{ed} is simply the distance along the surface from the origin in the surface reflectance data.

C. Monte Carlo Algorithm

The publicly available MCML and CONV programs implement Monte Carlo simulation of a multi-layer model of a cylindrically symmetrical geometry with adjustable spatial dimensions and resolution [23], [24]. The source code files [25] were downloaded, and executable versions built utilizing the Borland C++ compiler, version 5.5, to operate on a personal computer. The only changes made to the source code resolved minor syntactic problems, expanded the resolution of ASCII output fields from 12 digits with 4 decimal places to 16 digits with 8 decimal places. The resulting programs were validated by examination of results from published test cases.

The dimensions and resolution of the model's grid were: depth $z, 0 \leq z \leq 1$ cm, $\Delta z = 0.002$ cm; radius $r, 0 \leq r \leq 3$ cm, $\Delta r = 0.01$ cm; and exit angle $\alpha, 0 \leq \alpha \leq 90$ deg, $\Delta\alpha = 1$ deg. Thus, the thinnest layers (epidermis and the bloodless dermis immediately below) were each 10 grid elements thick. The resolution employed should be sufficient for accurate representation of photon travel, given that the mean free path $(1/(\mu_a + \mu_s))$ ranges from 0.012–0.022 cm, and the transport mean free path $(1/(\mu_a + \mu_s'))$ ranges from 0.03–0.11 cm, for the conditions of Tables I–II.

A Microsoft Excel™ spreadsheet, MetaMCML, was used to generate the input (.mci) files for MCML. This spreadsheet incorporated the geometrical parameters, absorbance and scattering coefficients for the tissue components, and physiological parameters such as oxygen saturation, arterial-venous saturation difference, melanin content, etc. Both one-layer and multilayer models were implemented.

The MCML surface reflectance output was post-processed with the CONV program to achieve emitter simulation by beam convolution. (The exit angle of emergent photons was not considered; i.e., the assumption was made that all photons emerging under the detector were collected.) The convolved surface reflectance data $S(r)$, the fraction of photons reaching the surface per cm^2 as a function of radial distance from the origin r, was

imported into a Microsoft Excel™ spreadsheet for further processing.

As dictated by MCML, the emitters are point sources centered at the origin $(r, z) = (0, 0)$, and normal to the tissue surface. The detector was simulated in the spreadsheet by calculating the average $S(r)$ in a sliding window equal to the width of the simulated detector, 0.2 cm. Multiplied by the detector area, 0.04 cm^2, this gives the detected surface reflectance $S_d(r)$, i.e., the fraction of photons reaching a detector centered at distance r from the emitters. The range of emitter-detector spacing was restricted to approximately $0.5 < r_{\rm ed} < 2.5$ cm, as a result of the convolution calculation ([24]) and the sliding sum employed in the detector simulation.

Normalized pulsatile reflectance was computed as the difference between diastolic S_d and systolic S_{dS}; divided by the diastolic S_d, this yielded the normalized pulsatile amplitude

$$N_\lambda(r) = (S_d(r) - S_{dS}(r))/S_d(r). \tag{6}$$

The ratio of red to infrared N_λ for a given emitter-detector spacing $r_{\rm ed}$ gives R, the ratiometric relationship that is the basis of pulse oximetry calibration (SpO_2 versus R)

$$R = N_{\rm red}(r_{\rm ed})/N_{ir}(r_{\rm ed}). \tag{7}$$

Oxygen saturation calibration and accuracy results presented are for $r_{\rm ed} = 1.2$ cm, a separation employed in fetal pulse oximetry.

Since pulse oximetry requires at least two wavelengths simulated under diastolic and systolic conditions, at least four simulation runs must be made for each oxygen saturation level studied under a given set of tissue conditions. Each simulation run consisted of $n = 2 \times 10^7$ photons and required approximately 2.5 h of processing time on a personal computer operating at a 1-GHz clock speed.

In some runs, the surface reflectance fractions became low enough at high $r_{\rm ed}$ to compromise calculation of N_λ. An empirical quality limit S_q was set equaling the minimum fraction of photons in the surface reflectance data

$$S_q = (n_d/(d/\Delta r))/n \tag{8}$$

based upon an arbitrary minimum number of photons reaching the detector, n_d; the size of the detector d expressed in radial grid units Δr; and the number of photons n in the run. The value of n_d was estimated as the minimum necessary to permit reliable calculation of N_λ as a difference, based upon test runs. For $n_d = 100$ photons and $n = 2 \times 10^7$ photons, $S_q = 2.5 \times 10^{-7}$. Several cases failing this test required averaging of the surface reflectance data from multiple runs (effectively raising n for certain cases), performed in the post-processing spreadsheet. (MCML employs the system time function to derive a seed for its random number generation; subsequent runs with identical input parameters were never observed to duplicate previous results.)

IV. Results

MCML runs were performed representing the full range of oxygen saturation for diastolic and systolic states and nominal versus reduced blood fraction, for both single-layer and multilayer models. The effect of melanin content was separately studied for a selected oxygen saturation value.

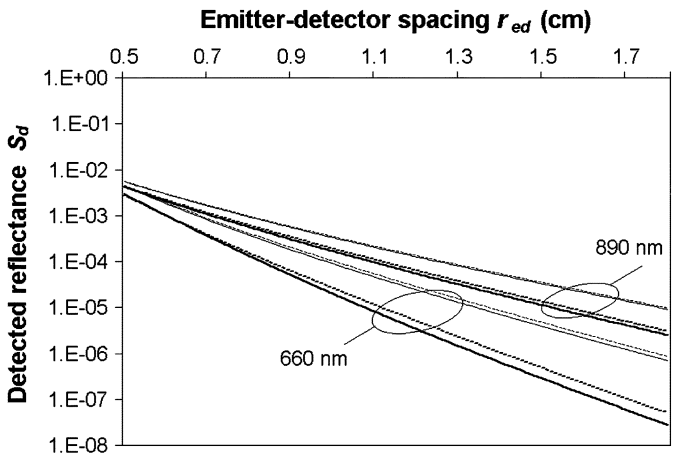

Fig. 2. S_d versus $r_{\rm ed}$ for 660 and 890 nm light at 20% SpO_2: nominal (dark) and reduced (light) blood fractions; single-layer (dashed) and multilayer (solid) models.

A. Surface Reflectance

The detected surface reflectance S_d versus emitter-detector spacing $r_{\rm ed}$ is shown in Fig. 2, for 660 and 890 nm. The curves represent nominal and reduced blood fractions with 20% SpO_2, from both the single-layer and multilayer models.

The magnitude of S_d falls exponentially with increasing $r_{\rm ed}$, beyond the vicinity of the emitter, as previously found [14]. An increase in blood fraction results in increasingly negative slopes, and a decrease in light reaching the detector under the far-detector condition. At low SpO_2 values, the red S_d is lower than infrared. The multilayer curves also exhibit a lower slope than single-layer in the far-detector condition.

B. Normalized Pulsatile Amplitude

N_λ versus emitter-detector spacing $r_{\rm ed}$ is shown in Fig. 3, for 660 and 890 nm. The curves represent nominal and reduced blood fractions with 20% SpO_2, from both the single-layer and multilayer models.

The magnitude N_λ rises with increasing $r_{\rm ed}$, an effect noted in laboratory and clinical studies [16], [26]. In the far-detector range of $0.5 < r_{\rm ed} < 2.5$ cm the single-layer curve appears to continue rising linearly, whereas the slope of the multilayer curve peaks, then decreases. Curves for other tissue states (not shown), including varying oxygen saturation, relative pulse size, and depth of the arterial pulsatility, reveal a consistently sigmoidal form with variation in magnitude and r of maximum slope $({\rm d}N_\lambda/{\rm d}r)$, and the asymptotic value of N_λ.

To test the hypothesis that single-layer and multilayer N_λ curves are fundamentally different, the data was fitted to linear and sigmoidal equations. (The sigmoidal form was approximated with a quartic polynomial.) The correlation for all curves was computed, and the goodness of fit assessed with the F test. For $0.5 < r_{\rm ed} < 2.0$ cm, Excel LINEST fits the single-layer and multilayer curves found in Fig. 3 to linear and quartic forms, respectively, with high correlations and $p < 0.01$, but fits the multilayer data to linear forms with lower correlations and $p > 0.01$ (Table III).

The ratiometric relationship $R = N_{\rm red}/N_{\rm IR}$ for linear N_λ curves is independent of emitter-detector spacing if the curves

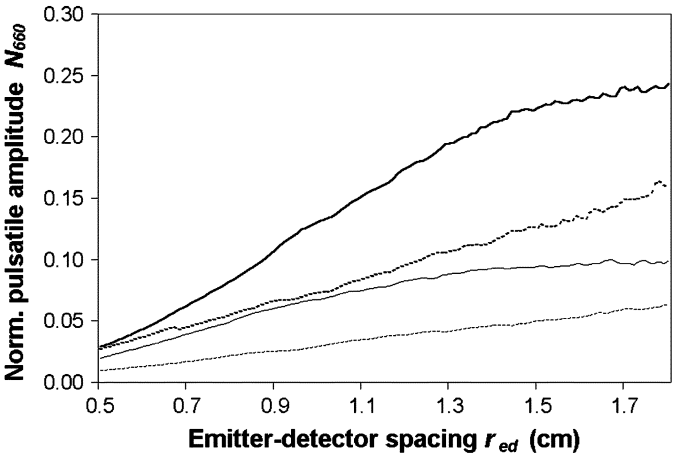

(a)

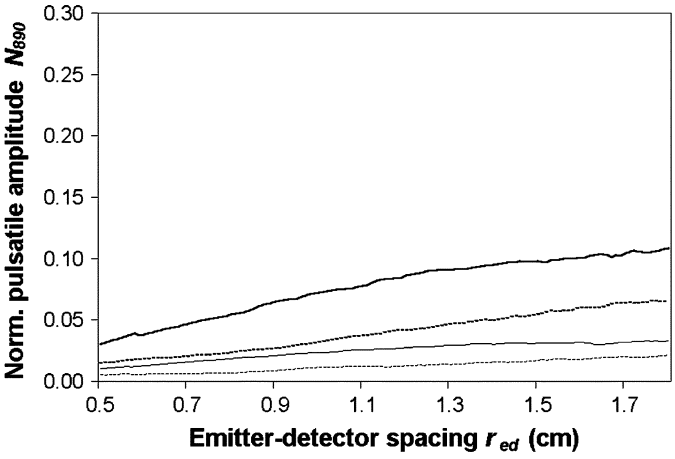

(b)

Fig. 3. N_λ versus $r_{\rm ed}$ for (a) 660 and (b) 890 nm wavelengths at 20% SpO_2: nominal (dark) and reduced (light) blood fractions; single-layer (dashed) and multilayer (solid) models.

TABLE III
N_λ CURVE FITS FOR SpO_2 AT 20%, $r_{\rm ed} > 0.5$ CM

f_0	model	curve fit	r^2, p λ=660 nm	r^2, p λ=890 nm
0.05	single-layer	linear*	0.995, 0.004	0.995, 0.005
	multilayer	linear	0.945, 0.016	0.957, 0.014
		quartic*	0.999, 0.004	0.999, 0.005
0.0125	single-layer	linear*	0.997, 0.004	0.989, 0.007
	multilayer	linear	0.899, 0.022	0.935, 0.017
		quartic*	0.998, 0.006	0.979, 0.009

* Significant at $p < 0.01$.

pass through the origin. This possibility was examined by forcing the intercepts to zero for single-layer data linear curve fits (not shown). Correlations and F test significance fell, yet in all cases remained $r^2 > 0.95$ and $p < 0.014$.

C. Ratiometric Relationship and Calibration

The ratio $R = N_{660}/N_{890}$ is related not only to the oxygen saturation but also the diastolic blood fraction, pulsatile blood fraction, blood characteristics, and tissue geometry. The impact of blood fraction is illustrated in Fig. 4, showing the ratio R versus oxygen saturation SaO_2 for $r_{\rm ed} = 1.2$ cm. These oximeter calibration curves are shown for nominal and reduced

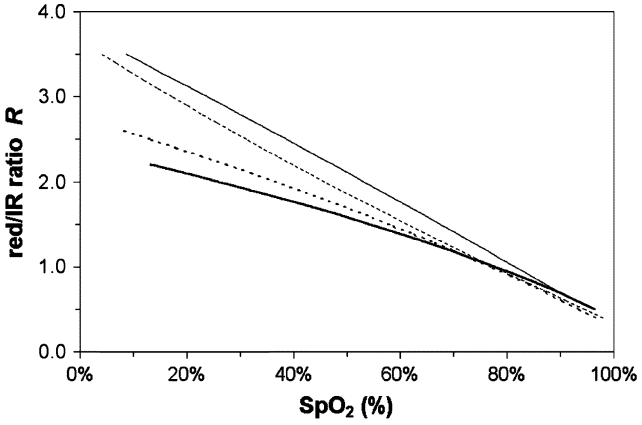

Fig. 4. R versus SpO_2 (%) for $r_{\rm ed} = 1.2$ cm: nominal (dark) and reduced (light) blood fractions; single-layer (dashed) and multilayer (solid) models.

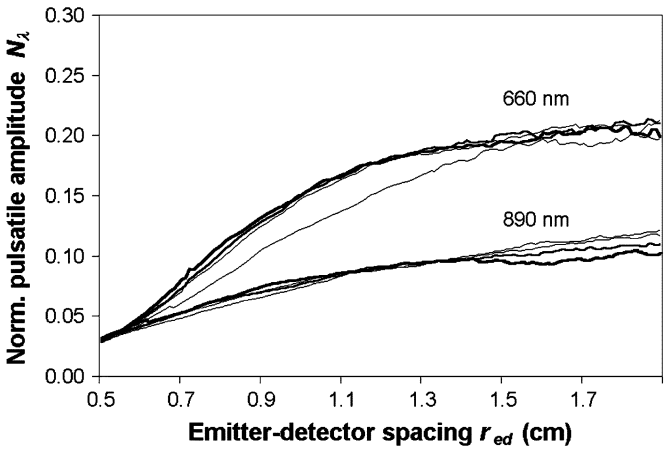

Fig. 5. N_λ versus $r_{\rm ed}$ for 660 (top) and 890 nm (bottom) wavelengths at 40% SpO_2 and nominal blood fraction in the multilayer model; 0% (lightest) to 20% (darkest) melanin fraction.

blood fractions over the range of 20%–100% oxygen saturation, for the single-layer and multilayer models. A reduction in blood fraction is predicted to shift the calibration curve, resulting in an underestimation of the oxygen saturation if the nominal calibration relationship is used.

Results for the single-layer model resemble those previously obtained for single-layer photon diffusion and Monte Carlo models [11], [18], indicating an increasing calibration error with reduction in blood fraction occurring at relatively low (<70% SaO_2) oxygen saturation levels. Notably, the multilayer model predicts an error in oxygen saturation calculation over a broader SaO_2 range for the same blood reduction. Previously published single-layer results exhibit higher slopes [18]; possible factors contributing to this include an assumption of isotropic scattering, use of a smaller simulated pulse, and/or different assumptions about melanin content (see below) in the previous results.

D. Melanin Content

The effect of varying melanin content in the multilayer tissue model was studied for 0%, 5%, 10%, and 20% melanin as the fraction of epidermal volume. Fig. 5 shows N_λ versus $r_{\rm ed}$ for

TABLE IV
EFFECT OF MELANIN ON CALIBRATION AT 40% SpO_2, $r_{ed} = 1.2$ CM

f_{mel}	R^a	SpO_2	$d(SpO_2)$
5%	1.985	39.3%	-0.694%
10%	1.965	40.5%	0.530%
20%	1.971	40.2%	0.164%
mean	1.973	40.0%	0.000%
S.D.	0.010	0.63%	0.63%
A(RMS)			0.51%

[a] Calibrated to average melanin content; see text.

nominal blood fraction and 40% oxygen saturation with the various melanin levels.

A substantial difference is apparent between the melanin-free state and the presence of melanin. Even a small melanin fraction creates a highly absorbing layer. The absorbance of 660 nm light by melanin is over 900 times greater than absorbance of the same wavelength by blood- and melanin-free tissue. The ratio of red to infrared absorbance by blood- and melanin-free tissue is only 1.16, whereas the red to infrared absorbance ratio of melanin is over 2.7 (Table I). Thus, the presence of even a small melanin fraction shifts the optical characteristics of the epidermal layer to relatively higher red versus infrared absorbance.

Variation in melanin over 5%–20% does not result in a significant change in the balance of red to infrared absorption. This was tested with an analysis of differences for a simulated calibration ($r_{ed} = 1.2$ cm) at the average of a population uniformly divided between 5%, 10%, and 20% melanin. As seen in Table IV, for the same population of 5%–20% melanin this results in an RMS error of 0.51% for the SpO_2 value of 40%, well within accuracy specifications for pulse oximetry in the low oxygen saturation range.

V. DISCUSSION

The N_λ versus r_{ed} curve has a sigmoidal shape in the multilayer model results. This reflects the localization of arterial pulsatility in depth. Although pulsatility of real tissue is not as neatly isolated, pulsatile pressure clearly is highest in the arterioles and drops to negligible levels in capillary plexus flow. The linearity of the single-layer model N_λ versus r_{ed} relationship could incorrectly imply that calibration is independent of emitter-detector spacing, when in fact experimental evidence indicates that R rises with increasing r_{ed} [14], [16]. Beyond 2.5 cm, it cannot be determined from the multilayer simulations described herein whether the pulse amplitudes remain constant, rise, or fall. Certainly the sigmoidal N_λ characteristic contributes to the complexity of the ratiometric relationship versus emitter-detector spacing.

The characteristic of the normalized pulsatile amplitude versus emitter-detector spacing relationship has potential impact upon pulse oximeter and sensor design. As previously suggested, increased emitter-detector spacing may result in increased sampling of deeper layers [27]. The importance of matching the depth of photon penetration in determining pulse oximetry accuracy [28] may diminish as the emitter-detector spacing is increased, if indeed pulsatile amplitudes approach constancy. However, the problems of signal strength and variation in tissue structure grow with increased detector spacing. Selection of wavelengths to guarantee similar depth of light penetration [18] should be based upon a model that realistically represents the localization in depth of arterial pulsatility. Various proposals to employ multiple emitter-detector spacings in order to reduce the impact of changes in tissue characteristics cannot assume a linear relationship of the normalized pulse amplitude with r_{ed}.

The multilayer model results suggest that blood fraction changes have a more significant impact on pulse oximeter calibration at higher oxygen saturations than concluded from the single-layer model. Conversely, this may indicate that blood fraction changes *in vivo* are not as great as those assumed in the referenced modeling studies. Experimental data collected to assess calibration accuracy under varying tissue sites [18] unfortunately has not included measurement of *in situ* diastolic blood fraction and/or arterial pulsatile fraction; empirical evidence to support the predictions of the multilayer model results remains to be obtained.

The difference between N_λ curves for $f_{mel} = 0$ versus $f_{mel} > 0$ likely lies in a change to the distribution through tissue of detected photon paths. The highly absorbent epidermis may tend to eliminate shallow travel through the tissue between emitter and detector, with relatively more detected photons passing through deeper (and more pulsatile) tissue. As noted, even a small melanin fraction in the epidermis tends to raise normalized pulsatile amplitudes where shallow travel is most likely, nearer to the emitter, versus the melanin-free case. Confirmation of this hypothesis requires further investigation utilizing photon tracking in light-tissue simulations. The absence of melanin in the multilayer model for studies of blood fraction variation probably shifts all the calibration relationships to slightly lower curves versus empirical observations. For the purpose of comparison with the single-layer model, however, this was a necessary simplification unlikely to change the comparison with single-layer results (which were also melanin-free).

Based upon the similarity of pulsatile amplitude results for $f_{mel} > 0$, calibration should be little affected by melanin content. As long as some melanin is present in the epidermis both at calibration and application, it appears that variation in melanin content over the rather broad range found in humans should not have a significant impact on pulse oximeter accuracy. Some clinical observations were probably confounded with equipment errors resulting from the reduced signal-noise ratio caused by diminished *absolute* pulsatile signal amplitudes in the presence of increased superficial absorption, whether physiologic or artificially induced. The results illustrated in Fig. 5 support conclusions previously drawn from laboratory measurements of reflectance versus skin color [29], suggesting that the weak signals obtained due to dark skin pigmentation can be improved with increased illumination.

The technique used to model melanin may shed light on the effects of other superficial interfering substances such as nail polish in adult monitoring, and meconium (a fetal excretory product which may stain the skin or amniotic membranes) in intrapartum monitoring. The degree of interference should be predictable from the difference between a superficial interfering substance's absorption characteristics at the wavelengths used

by the oximeter and those of melanin, the dominant superficial absorber.

Future work should explore other factors, including the size of the pulsatile blood fraction, depth of the pulsatile layer, and impact of palpably large superficial vessels. Further development of MCML can make it possible to collect photon migration paths and calculate mean path length, depth of penetration, and other statistics. The assumptions about anisotropy and refractive index per layer (including the impact of specular reflectance at the sensor-tissue interface, related to skin health), should be evaluated. The dependency of light scattering in tissue on collagen alignment [21] (related to the maturity of the skin [30]), and in blood on flow rate and direction [22] should also be explored.

VI. Conclusion

The multilayer model of reflectance pulse oximetry affirms the dependence of calibration upon blood fraction, but also the importance of pulse fraction and localization of pulsatility. The insensitivity of pulse oximetry to melanin content is supported by the simulation results. Conclusions drawn about pulse oximetry from homogenous models of the behavior of light in tissue should be re-examined, especially as they impact equipment design.

References

[1] J. F. Kelleher, "Pulse oximetry," *J. Clin. Monit.*, vol. 5, no. 1, pp. 37–62, 1989.

[2] C. D. Kurth, J. M. Steven, and D. Swedlow, "New frontiers in oximetry," *Am. J. Anesthesiol.*, vol. 23, pp. 169–175, 1996.

[3] G. A. Dildy, J. A. Thorp, J. D. Yeast, and S. L. Clark, "The relationship between oxygen saturation and pH in umbilical blood: Implications for intrapartum fetal oxygen saturation monitoring," *Am. J. Obstet. Gynecol.*, pt. 1, vol. 175, no. 3, pp. 682–687, 1996.

[4] A. K. Luttkus, J. H. Stupin, M. Porath, and J. W. Dudenhausen, "Evaluation of signal quality of a new fetal pulsoximetry system (OBS-500). A recent development of a fetal oxisensor positioned on the fetal back," *J. Perinat. Med.*, vol. 29, no. S1, p. 251, 2001.

[5] J. L. Reuss and D. Siker, "Monitoring site and wavelength selection for fetal pulse oximetry," presented at the Annu. Meeting Assoc. Advanc. Med. Instr., Baltimore, MD, June 2001.

[6] J. L. Reuss, "Factors influencing fetal pulse oximetry performance," *J. Clin. Monit. Comput.*, vol. 18, no. 1, pp. 13–24, 2004.

[7] K. Kramer, J. O. Elam, G. A. Saxton, and W. N. Elam Jr., "Influence of oxygen saturation, ethryocyte concentration and optical depth upon the red and near-infrared light transmittance of whole blood," *Am. J. Physiol.*, vol. 165, pp. 229–46, 1951.

[8] C. Davies, S. Takatani, N. Sakakibara, and Y. Nose, "Application of the Kubelka Munk equation to characterizing a reflectance pulse oximeter," in *Proc. Int. Conf. IEEE Eng. Med. Biol. Soc.*, vol. 4, 1989, pp. 1095–1097.

[9] J. M. Steinke and A. P. Shepherd, "Role of light scattering in whole blood oximetry," *IEEE Trans. Biomed. Eng.*, vol. 33, no. 3, pp. 294–301, Mar. 1986.

[10] D. R. Marble and P. W. Cheung, "Mathematical model of transmission pulse oximetry," in *Proc. Annu. Int. Conf. IEEE Eng. Med. Biol. Soc.*, vol. 2, 1988, pp. 542–543.

[11] J. M. Schmitt, "Simple photon diffusion analysis of the effects of multiple scattering on pulse oximetry," *IEEE Trans. Biomed. Eng.*, vol. 38, no. 12, pp. 1194–1203, Dec. 1991.

[12] D. R. Marble, D. H. Burns, and P. W. Cheung, "Diffusion-based model of pulse oximetry: *In vitro* and *in vivo* comparisons," *Appl. Opt.*, vol. 33, no. 7, pp. 1279–1285, 1994.

[13] S. Takatani and M. D. Graham, "Theoretical analysis of diffuse reflectance from a two-layer tissue model," *IEEE Trans. Biomed. Eng.*, vol. 26, no. 12, pp. 656–664, Dec. 1979.

[14] J. M. Schmitt, G. X. Zhou, E. C. Walker, and R. T. Wall, "Multilayer model of photon diffusion in skin," *J. Opt. Soc. Am. A*, vol. 7, no. 11, pp. 2141–2153, 1990.

[15] M. J. van Gemert, S. L. Jacques, H. J. Sterenborg, and W. M. Star, "Skin optics," *IEEE Trans. Biomed. Eng.*, vol. 36, no. 12, pp. 1146–1154, Dec. 1989.

[16] R. Graaff, A. C. Dassel, W. G. Zijlstra, F. F. de Mul, and J. G. Aarnoudse, "How tissue optics influences reflectance pulse oximetry," *Adv. Exp. Med. Biol.*, vol. 388, pp. 117–132, 1996.

[17] V. V. Tuchin, "Light scattering study in tissues," *Physics—Uspekhhi*, vol. 40, no. 5, pp. 495–515, 1997.

[18] P. D. Mannheimer, J. R. Casciani, M. E. Fein, and S. L. Nierlich, "Wavelength selection for low-saturation pulse oximetry," *IEEE Trans. Biomed. Eng.*, vol. 44, no. 3, pp. 148–158, Mar. 1997.

[19] S. L. Jacques, "Skin optics," *Oregon Med. Laser Center News*, no. 1, pp. 1–9, Jan. 1998.

[20] S. L. Jacques and D. J. McAuliffe, "The melanosome: Threshold temperature for explosive vaporization and internal absorption coefficient during pulsed laser irradiation," *Photochem. Photobiol.*, vol. 53, no. 6, pp. 769–75, 1991.

[21] S. Nickell, M. Hermann, M. Essenpreis, T. J. Farrell, U. Kramer, and M. S. Patterson, "Anisotropy of light propagation in human skin," *Phys. Med. Biol.*, vol. 45, no. 10, pp. 2873–86, 2000.

[22] A. M. Enejder, J. Swartling, P. Aruna, and S. Andersson-Engels, "Influence of cell shape and aggregate formation on the optical properties of flowing whole blood," *Appl. Opt.*, vol. 42, no. 7, pp. 1384–94, 2003.

[23] L. Wang, S. L. Jacques, and L. Zheng, "MCML—Monte Carlo modeling of light transport in multi-layered tissues," *Comput. Methods Programs Biomed.*, vol. 47, no. 2, pp. 131–146, 1995.

[24] L. Wang, S. L. Jacques, and L. Zheng, "CONV—Convolution for responses to a finite diameter photon beam incident on multi-layered tissues," *Comput. Methods Programs Biomed.*, vol. 54, no. 3, pp. 141–150, 1997.

[25] L. Wang and S. L. Jacques, "Monte Carlo Simulation Package Release 5: MCML 1.2.2 & CONV 1.1.," Texas A&M Univ., College Station, TX, [Online]. Available: http://oilab.tamu.edu/mc.html, Mar. 2000.

[26] J. Ling, S. Takatani, G. P. Noon, and Y. Nose, "*In-vivo* studies of reflectance pulse oximeter sensor," *Physiologic. Imag., Spectroscopy, Early Detection Diagnostic Meth.*, vol. 1887, pp. 256–262, 1993.

[27] W. J. Cui and L. E. Ostrander, "The relationship of surface reflectance measurements to optical properties of layered biological media," *IEEE Trans. Biomed. Eng.*, vol. 39, no. 2, pp. 194–201, Feb. 1992.

[28] P. D. Mannheimer, M. E. Fein, and J. R. Casciani, "Physio-optical considerations in the design of fetal pulse oximetry sensors," *Eur. J. Obstet. Gynecol. Reprod. Biol.*, vol. 72, no. Suppl, pp. S9–19, 1997.

[29] W. J. Cui, L. E. Ostrander, and B. Y. Lee, "*In vivo* reflectance of blood and tissue as a function of light wavelength," *IEEE Trans. Biomed. Eng.*, vol. 37, no. 6, pp. 632–9, June 1990.

[30] I. S. Saidi, S. L. Jacques, and F. K. Tittel, "Mie and Rayleigh modeling of visible-light scattering in neonatal skin," *Appl. Opt.*, vol. 34, no. 31, pp. 7410–7418, 1995.

James L. Reuss (S'76–M'81–SM'02) received the S.B. degree in life sciences from the Massachusetts Institute of Technology, Cambridge, MA, in 1973, the M.S. in bioengineering from the University of Illinois, Chicago, in 1976, and the Ph.D. in biomedical engineering from Northwestern University, Evanston, IL, in 1981.

He is currently the Vice-President of Research & Development at OB Scientific, Inc. , Germantown, WI, where he is responsible for fetal pulse oximetry. Previously, he was employed by Criticare Systems, Inc., where he developed the ComfortCuff™ NIBP and DOX™ digital oximetry technologies. He holds patents in medical devices, including pulse oximetry and medical telemetry; his professional interests include physiological signal processing and development of noninvasive medical sensing and imaging modalities.